Handong Li
Jiang Wu
Zhiming M. Wang   *Editors*

Silicon-based Nanomaterials

Springer

Editors
Handong Li
Jiang Wu
Zhiming M. Wang
State Key Laboratory of Electronic
 Thin Film and Integrated Devices
University of Electronic Science
 and Technology of China
Chengdu
People's Republic of China

Chapter 3
Light Trapping in Coaxial Nanowires of c-Si Cores and a-Si Shells

Jeong Il Oh, Wenfu Liu, Weiqiang Xie and Wenzhong Shen

Abstract Light absorption is investigated in coaxial nanowires (NWs) of crystalline silicon (c-Si) cores and amorphous silicon (a-Si) shells, including both cases of single coaxial NWs and coaxial NW arrays, for an incident light spectrum of 1.0–4.0 eV covering the major solar band for photovoltaic cells. Based on the Lorenz-Mie light scattering theory for the single coaxial NWs and the rigorous coupled-wave analysis method for the coaxial NW arrays, it is found that the incident light is effectively trapped in the coaxial NWs through absorption resonances so that the light absorption of the coaxial NWs can be significantly enhanced compared to that of c-Si NWs. In the coaxial NWs, the absorption resonances occur due to their subwavelength dimensions, as in the c-Si NWs, whereas the absorption enhancement originates from the a-Si shells. By tuning their structural parameters, the light absorption in the coaxial NWs can be readily optimized for photovoltaic applications. At the optimal absorption conditions, the photocurrent in the coaxial NWs can be enhanced up to 560 % (single case) and 14 % (array case) compared to that in the c-Si NWs. The underlying physics of the light absorption in the coaxial NWs is discussed in terms of the excitation of leaky-mode resonances. The practical use of the coaxial NWs for photovoltaic cells is also addressed.

3.1 Introduction

Light trapping is a very important technology to increase the light absorption of and thereby to enhance the power conversion efficiency of photovoltaic (PV) cells [1–35]. Surface texturing combined with front-surface antireflection coating and rear-surface reflector is conventionally used to elongate the optical path length of the incident light

J. I. Oh · W. F. Liu · W. Q. Xie · W. Z. Shen (✉)
Laboratory of Condensed Matter Spectroscopy and Opto-Electronic Physics,
Key Laboratory of Artificial Structures and Quantum Control (Ministry of Education),
Department of Physics and Institute of Solar Energy, Shanghai Jiao Tong University,
800 Dong Chuan Road, Shanghai 200240 , China
e-mail: wzshen@sjtu.edu.cn

in commercial PV cells [2], whereas light interaction with subwavelength-scaled matters is becoming a new approach to effective light trapping for next generation PV cells, including plasmonic PV cells [3–8], thin-film PV cells with submicron-sized light scatterers [9], and NW-based PV cells [10–35]. Among these, the latter PV cells, especially based on c-Si NWs [15–35], have recently drawn considerable attention because of their great potential to reduce the cost of the power generation mainly owing to the new light-trapping scheme.

Sunlight can be effectively trapped in c-Si NWs mainly through absorption resonances, leading to significant absorption enhancement compared to the bulk counterparts. The absorption resonances originate from the interaction between the incident sunlight and subwavelength-scaled c-Si NWs. [32–34] The light absorption in c-Si NWs can exceed the conventional Lambertian limit of light trapping [35–38] so that the light-trapping scheme in c-Si NWs is particularly important in designing next generation PV cells based on Si nanomaterials. The light absorption in c-Si NWs can be further enhanced by coating highly absorptive a-Si shells. [29] These hybrid NWs of coaxial structure, comprising c-Si cores and a-Si shells, would be very attractive since they could take advantage of superior light absorption property of a-Si [39] while retaining long charge carrier diffusion lengths of c-Si ($>200\,\mu$m) [40]. More specifically, in PV cells made of such coaxial NWs of c-Si cores and a-Si shells, the Si cores could serve as an efficient charge collector [41] to compensate for short diffusion lengths of a-Si (~100 nm) [40], and the a-Si shells could be used not only as an excellent surface passivator [42] but also as an excellent energy absorber to overcome rather poor light absorption of c-Si [39].

In this chapter, the light absorption and its underlying mechanism in the coaxial NWs of c-Si cores and a-Si shells are investigated for both cases of single coaxial NWs and coaxial NW arrays, based on the Lorenz-Mie light scattering theory [43] and the rigorous coupled-wave analysis method [44–46], respectively. Three important findings of this investigation are: (1) The excitation of LMRs governs the light absorption in the coaxial NWs; (2) the significant absorption enhancement in the coaxial NWs, as compared to that in the c-Si NWs, stems from the a-Si shells; and (3) the dimensions of the coaxial NWs can be optimally tuned for PV applications. This chapter will first describe the calculation methods of the light absorption in the coaxial NWs in the next section, extensively deal with the light trapping mechanism in the coaxial NWs and its potential uses in PV applications in the following two sections, and close with the summary and conclusions at the last section.

3.2 Light Absorption Calculation Methods

3.2.1 Lorentz-Mie Scattering Theory

The light absorption efficiency of single NWs can be calculated as follows: Within the framework of the Lorentz-Mie light scattering theory, where single NWs are treated as infinitely long cylinders, normally illuminated by a plane wave of the incident

propagation vector k_0 [43]. For unpolarized light, the light absorption efficiency Q_{abs}, defined as the ratio of the absorption cross section to the geometrical cross section of NWs, can be expressed as

$$Q_{abs} = (Q_{abs}^{TE} + Q_{abs}^{TM})/2, \qquad (3.1)$$

where Q_{abs}^{TE} and Q_{abs}^{TM} are the light absorption efficiencies for transverse-electric (TE, electric field perpendicular to the NW axis as in Fig. 3.1a) and transverse-magnetic (TM, electric field parallel to the NW axis as in Fig. 3.1a) illuminations, respectively. These are decomposed into

$$Q_{abs}^{TE} = Q_{ext}^{TE} - Q_{sca}^{TE}, \quad Q_{abs}^{TM} = Q_{ext}^{TM} - Q_{sca}^{TM}, \qquad (3.2)$$

where $Q_{ext}^{TE}(Q_{sca}^{TE})$ and $Q_{ext}^{TM}(Q_{sca}^{TM})$ are the extinction (scattering) efficiencies for TE and TM illuminations, respectively. These efficiencies are given by

$$Q_{ext}^{TE} = \frac{2}{k_0 r} \text{Re} \left\{ \sum_{n=-\infty}^{\infty} a_n \right\}, \quad Q_{ext}^{TM} = \frac{2}{k_0 r} \text{Re} \left\{ \sum_{n=-\infty}^{\infty} b_n \right\}, \qquad (3.3a)$$

$$Q_{sca}^{TE} = \frac{2}{k_0 r} \left\{ \sum_{n=-\infty}^{\infty} |a_n|^2 \right\}, \quad Q_{sca}^{TM} = \frac{2}{k_0 r} \left\{ \sum_{n=-\infty}^{\infty} |b_n|^2 \right\}, \qquad (3.3b)$$

where r is the radial dimension of the absorption part of a NW. In the case of a coaxial NW of Si core and SiO_2 shell (a case of Fig. 3.1b) under a major solar illumination (1.0–4.0 eV), for instance, r is r_2 but not r_1, since the bandgap of SiO_2 is over 4.0 eV so that the SiO_2 shell acts as a nonabsorbing medium in such a coaxial NW [13]. a_n and b_n can be readily obtained by solving Maxwell's equations with the appropriate boundary conditions at such interfaces as air/NW (Fig. 3.1a), air/shell and shell/core (Fig. 3.1b), and air/outer shell, outer shell/inner shell, and inner shell/core (Fig. 3.1c). The coefficients a_n and b_n can be written as

$$a_n = a_{n0}/\Delta_n^{TE}, \quad b_n = b_{n0}/\Delta_n^{TM}. \qquad (3.4)$$
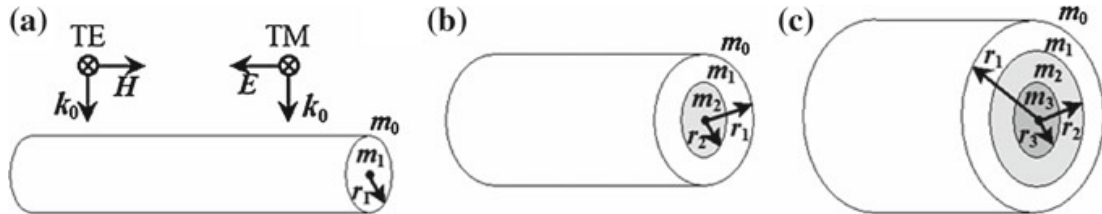
Fig. 3.1 Schematic diagrams of cylindrical NWs. Incident light polarizations with respect to the NW axis (TE and TM), radii (r), and complex refractive indices (m) are indicated. **a** Single material NW of r_1 and m_1. **b** Coaxial NW of core (r_2 and m_2) and shell ($r_1 - r_2$ and m_1). **c** Coaxial NW of core (r_3 and m_3), inner shell ($r_2 - r_3$ and m_2), and outer shell ($r_1 - r_2$ and m_1)

For single material NWs as in Fig. 3.1a,

$$a_{n0} = \begin{vmatrix} J_n'(k_0 r_1) & J_n'(k_1 r_1) \\ m_0 J_n(k_0 r_1) & m_1 J_n(k_1 r_1) \end{vmatrix}, \tag{3.5a}$$

$$\Delta_n^{\mathrm{TE}} = \begin{vmatrix} H_n'(k_0 r_1) & J_n'(k_1 r_1) \\ m_0 H_n(k_0 r_1) & m_1 J_n(k_1 r_1) \end{vmatrix}, \tag{3.5b}$$

$$b_{n0} = \begin{vmatrix} J_n(k_0 r_1) & J_n(k_1 r_1) \\ m_0 J_n'(k_0 r_1) & m_1 J_n'(k_1 r_1) \end{vmatrix}, \tag{3.5c}$$

$$\Delta_n^{\mathrm{TM}} = \begin{vmatrix} H_n(k_0 r_1) & J_n(k_1 r_1) \\ m_0 H_n'(k_0 r_1) & m_1 J_n'(k_1 r_1) \end{vmatrix}. \tag{3.5d}$$

For coaxial NWs of core/shell structure as in Fig. 3.1b,

$$a_{n0} = \begin{vmatrix} 0 & J_n'(k_1 r_2) & H_n'(k_2 r_2) & -J_n'(k_2 r_2) \\ 0 & m_1 J_n(k_1 r_2) & m_1 H_n(k_2 r_2) & -m_2 J_n(k_2 r_2) \\ J_n'(k_0 r_1) & J_n'(k_1 r_1) & H_n'(k_1 r_1) & 0 \\ m_0 J_n(k_0 r_1) & m_1 J_n(k_1 r_1) & m_1 H_n(k_1 r_1) & 0 \end{vmatrix}, \tag{3.6a}$$

$$\Delta_n^{\mathrm{TE}} = \begin{vmatrix} 0 & J_n'(k_1 r_2) & H_n'(k_1 r_2) & -J_n'(k_2 r_2) \\ 0 & m_1 J_n(k_1 r_2) & m_1 H_n(k_1 r_2) & -m_2 J_n(k_2 r_2) \\ H_n'(k_0 r_1) & J_n'(k_1 r_1) & H_n'(k_1 r_1) & 0 \\ m_0 H_n(k_0 r_1) & m_1 J_n(k_1 r_1) & m_1 H_n(k_1 r_1) & 0 \end{vmatrix}, \tag{3.6b}$$

$$b_{n0} = \begin{vmatrix} 0 & J_n(k_1 r_2) & H_n(k_2 r_2) & -J_n(k_2 r_2) \\ 0 & m_1 J_n'(k_1 r_2) & m_1 H_n'(k_2 r_2) & -m_2 J_n'(k_2 r_2) \\ J_n(k_0 r_1) & J_n(k_1 r_1) & H_n(k_1 r_1) & 0 \\ m_0 J_n'(k_0 r_1) & m_1 J_n'(k_1 r_1) & m_1 H_n'(k_1 r_1) & 0 \end{vmatrix}, \tag{3.6c}$$

$$\Delta_n^{\mathrm{TM}} = \begin{vmatrix} 0 & J_n(k_1 r_2) & H_n(k_1 r_2) & -J_n(k_2 r_2) \\ 0 & m_1 J_n'(k_1 r_2) & m_1 H_n'(k_1 r_2) & -m_2 J_n'(k_2 r_2) \\ H_n(k_0 r_1) & J_n(k_1 r_1) & H_n(k_1 r_1) & 0 \\ m_0 H_n'(k_0 r_1) & m_1 J_n'(k_1 r_1) & m_1 H_n'(k_1 r_1) & 0 \end{vmatrix}. \tag{3.6d}$$

For coaxial NWs of double shell structure as in Fig. 3.1c,

$$
a_{n0} = \begin{vmatrix}
0 & 0 & 0 & -J_n'(k_2 r_3) & -H_n'(k_2 r_3) & J_n'(k_3 r_3) \\
0 & 0 & 0 & -m_2 J_n(k_2 r_3) & -m_2 H_n(k_2 r_3) & m_3 J_n(k_3 r_3) \\
0 & J_n'(k_1 r_2) & H_n'(k_1 r_2) & -J_n'(k_2 r_2) & -H_n'(k_2 r_2) & 0 \\
0 & m_1 J_n(k_1 r_2) & m_1 H_n(k_1 r_2) & -m_2 J_n(k_2 r_2) & -m_2 H_n(k_2 r_2) & 0 \\
J_n'(k_0 r_1) & J_n'(k_1 r_1) & H_n'(k_1 r_1) & 0 & 0 & 0 \\
m_0 J_n(k_0 r_1) & m_1 J_n(k_1 r_1) & m_1 H_n(k_1 r_1) & 0 & 0 & 0
\end{vmatrix},
$$

(3.7a)

$$
\Delta_n^{\text{TE}} = \begin{vmatrix}
0 & 0 & 0 & -J_n'(k_2 r_3) & -H_n'(k_2 r_3) & J_n'(k_3 r_3) \\
0 & 0 & 0 & -m_2 J_n(k_2 r_3) & -m_2 H_n(k_2 r_3) & m_3 J_n(k_3 r_3) \\
0 & J_n'(k_1 r_2) & H_n'(k_1 r_2) & -J_n'(k_2 r_2) & -H_n'(k_2 r_2) & 0 \\
0 & m_1 J_n(k_1 r_2) & m_1 H_n(k_1 r_2) & -m_2 J_n(k_2 r_2) & -m_2 H_n(k_2 r_2) & 0 \\
H_n'(k_0 r_1) & J_n'(k_1 r_1) & H_n'(k_1 r_1) & 0 & 0 & 0 \\
m_0 H_n(k_0 r_1) & m_1 J_n(k_1 r_1) & m_1 H_n(k_1 r_1) & 0 & 0 & 0
\end{vmatrix},
$$

(3.7b)

$$
b_{n0} = \begin{vmatrix}
0 & 0 & 0 & -J_n(k_2 r_3) & -H_n(k_2 r_3) & J_n(k_3 r_3) \\
0 & 0 & 0 & -m_2 J_n'(k_2 r_3) & -m_2 H_n'(k_2 r_3) & m_3 J_n'(k_3 r_3) \\
0 & J_n(k_1 r_2) & H_n(k_1 r_2) & -J_n(k_2 r_2) & -H_n(k_2 r_2) & 0 \\
0 & m_1 J_n'(k_1 r_2) & m_1 H_n'(k_1 r_2) & -m_2 J_n'(k_2 r_2) & -m_2 H_n'(k_2 r_2) & 0 \\
J_n(k_0 r_1) & J_n(k_1 r_1) & H_n(k_1 r_1) & 0 & 0 & 0 \\
m_0 J_n'(k_0 r_1) & m_1 J_n'(k_1 r_1) & m_1 H_n'(k_1 r_1) & 0 & 0 & 0
\end{vmatrix},
$$

(3.7c)

$$
\Delta_n^{\text{TM}} = \begin{vmatrix}
0 & 0 & 0 & -J_n(k_2 r_3) & -H_n(k_2 r_3) & J_n(k_3 r_3) \\
0 & 0 & 0 & -m_2 J_n'(k_2 r_3) & -m_2 H_n'(k_2 r_3) & m_3 J_n'(k_3 r_3) \\
0 & J_n(k_1 r_2) & H_n(k_1 r_2) & -J_n(k_2 r_2) & -H_n(k_2 r_2) & 0 \\
0 & m_1 J_n'(k_1 r_2) & m_1 H_n'(k_1 r_2) & -m_2 J_n'(k_2 r_2) & -m_2 H_n'(k_2 r_2) & 0 \\
H_n(k_0 r_1) & J_n(k_1 r_1) & H_n(k_1 r_1) & 0 & 0 & 0 \\
m_0 H_n'(k_0 r_1) & m_1 J_n'(k_1 r_1) & m_1 H_n'(k_1 r_1) & 0 & 0 & 0
\end{vmatrix},
$$

(3.7d)

where J_n is the nth-order Bessel function of the first kind, and H_n is the nth-order Hankel function of the first kind. The prime superscript stands for differentiation with respect to the propagation vector $k_i = m_i k_0$ ($i = 0, 1, 2,$ and 3) for the air environment ($m_0 = 1$). It is worth noting that the optical properties of single NWs retain qualitatively same for a wide range of the angle of incident light so that the angle of incident does not play an important role in designing NW-based optical devices [32, 47].

3.2.2 Rigorous Coupled-Wave Analysis

The light absorption of coaxial NW arrays can be calculated by the rigorous coupled-wave analysis (RCWA) method [44–46]. It has been initially developed for calculating the diffraction orders of one-dimensional (1D) gratings by solving Maxwell's
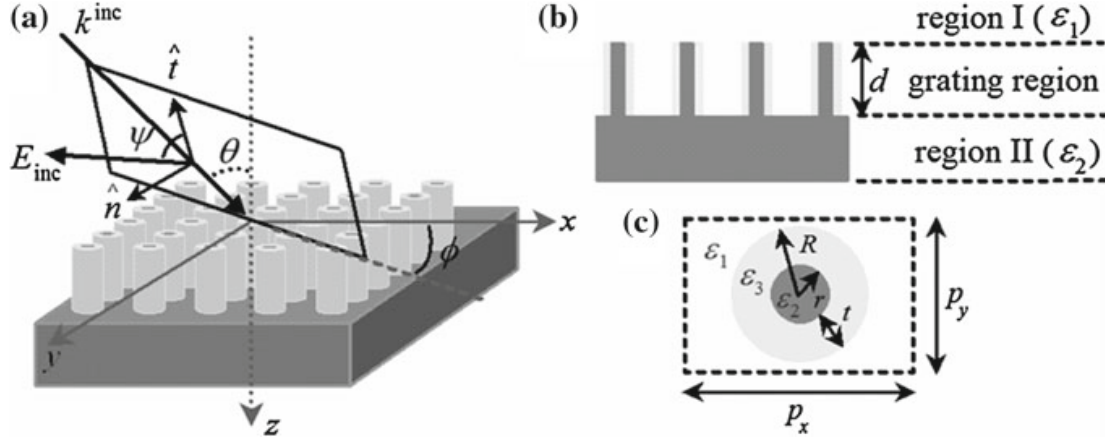
Fig. 3.2 Schematic illustrations of a 2D grating, comprising a rectangular array of coaxial pillars with periodicities p_x and p_y. **a** Incident light (k^{inc}) and electric field (E_{inc}) are shown with respect to the grating. **b** *Side view* of the grating, showing three regions of the grating. **c** *Top view* of the unit cell of the grating

equations and later extended to two-dimensional (2D) periodic structures with sub-wavelength scale such as surface-relief gratings [46] and periodic nanostructures [48]. As a frequency-domain simulation, it can readily incorporate material dispersion, thereby offering reflectance (R), transmittance (T), and absorptance (A) for investigating the optical properties of subject materials. The RCWA approach to calculating the light absorption of coaxial NW arrays can be programmed as described in the following procedures.

Figure 3.2 illustrates a 2D NW pillar grating, consisting of three regions: The incident region or reflected region with the relative permittivity ε_1 (Region I), the transmitted region with ε_2 (Region II), and the grating region of a coaxial NW array with three relative permittivities whose geometric parameters are shown in Figs. 3.2b and 3.2c. A linearly polarized plane wave (k^{inc}) at an arbitrary angle of incidence (θ, ϕ) is considered. The angle between the electric field (E_{inc}) and the plane of incidence is denoted by ψ so that $\psi = 0°$ and $90°$ correspond to TE and TM polarizations, respectively. The periodic relative permittivity $\varepsilon(x, y)$ in the grating region ($0 < z < d$) can be expanded in a Fourier series as

$$\varepsilon(x, y) = \varepsilon(x + p_x, y + p_y) = \sum_{m,n} \varepsilon_{mn} \exp\left(j\frac{2\pi m x}{p_x} + j\frac{2\pi n y}{p_y} \right), \qquad (3.8)$$

where ε_{mn} is the (m,n)th Fourier coefficient, which is determined only by the geometry of the grating as shown in Fig. 3.2c. The electric-field vectors in the regions I and II are given by

$$E_I = E_{inc} + \sum_{m,n} R_{mn} \exp[-j(k_{x,m}x + k_{y,n}y - k^I_{z,mn}z)], \qquad (3.9a)$$

$$E_{\mathrm{II}} = \sum_{m,n} T_{mn} \exp\{-j[k_{x,m}x + k_{y,n}y + k_{z,mn}^{\mathrm{II}}(z-d)]\}, \qquad (3.9\mathrm{b})$$

where E_{inc} is the normalized incident electric-field vector (i.e., $|E_{\mathrm{inc}}|^2 = 1$) and $r_{mn}(T_{mn})$ is the normalized amplitude of electric-field vector in the (m,n)th reflected (transmitted) diffraction order. In Equations 3.9a and 3.9b, the components of wave vector are determined from the Floquet condition as

$$k_{x,m} = k_x^{\mathrm{inc}} - 2\pi m/p_x, \qquad (3.10\mathrm{a})$$

$$k_{y,n} = k_y^{\mathrm{inc}} - 2\pi n/p_y, \qquad (3.10\mathrm{b})$$

$$k_{z,mn}^i = \begin{cases} \sqrt{k_0^2 \varepsilon_i - (k_{x,m}^2 + k_{y,n}^2)} & (k_{x,m}^2 + k_{y,n}^2 < k_0^2 \varepsilon_i) \\ -j\sqrt{(k_{x,m}^2 + k_{y,n}^2) - k_0^2 \varepsilon_i} & (k_{x,m}^2 + k_{y,n}^2 > k_0^2 \varepsilon_i) \end{cases} \quad i = \mathrm{I} \text{ and } \mathrm{II}, $$

$$(3.10\mathrm{c})$$

where k^{inc} is the wave vector of the incident light and $k_0 = 2\pi/\lambda_0$ with λ_0 the wavelength of the incident light in free space. The electric- and magnetic-field vectors $(E_g$ and $H_g)$ in the grating region can be expressed in terms of the space-harmonic fields as

$$E_g = \sum_{m,n} S_{mn} \exp[-j(k_{x,m}x + k_{y,n}y)], \qquad (3.11\mathrm{a})$$

$$H_g = -j\left(\frac{\varepsilon_0}{\mu_0}\right)^{1/2} \sum_{m,n} U_{mn} \exp[-j(k_{x,m}x + k_{y,n}y)], \qquad (3.11\mathrm{b})$$

where S_{mn} and U_{mn} are the normalized amplitudes of the (m,n)th space-harmonic fields, ε_0 is the permittivity of free space, and μ_0 is the permeability of free space. E_g and H_g satisfy Maxwell's curl equations in the source-free space as

$$\nabla \times E_g = -j\omega\mu_0 H_g, \quad \nabla \times H_g = j\omega\varepsilon_0\varepsilon E_g. \qquad (3.12)$$

Inserting Equations 3.11a and 3.11b into 3.12, one can obtain a set of coupled-wave equations, which can be readily solved by applying the boundary conditions for electric- and magnetic-field components. The reflected and transmitted efficiencies for the (m,n)th diffraction order are defined as

$$\mathrm{DE}_{mn}^R = |R_{mn}|^2 \mathrm{Re}\left(\frac{k_{z,mn}^{\mathrm{I}}}{k_z^{\mathrm{inc}}}\right), \quad \mathrm{DE}_{mn}^T = |T_{mn}|^2 \mathrm{Re}\left(\frac{k_{z,mn}^{\mathrm{II}}}{k_z^{\mathrm{inc}}}\right) \qquad (3.13)$$

The total reflectance (R) and transmittance (T) are obtained by summing all diffraction orders as

$$R = \sum_{m,n} \mathrm{DE}_{mn}^R, \quad T = \sum_{m,n} \mathrm{DE}_{mn}^T \qquad (3.14)$$

For lossy dielectric materials, the total absorptance (A) is simply calculated by $A = 1 - R - T$. The accuracy of the RCWA simulation depends on the number of the space-harmonic fields retained in Equations 3.11a and 3.11b. It is worth noting that although it is a powerful simulation tool for periodic subwavelength structures, the RCWA method is also well applied to capturing the main optical properties of aperiodic structures by modeling the structures appropriately [49, 50].

3.3 Light Trapping in Single Coaxial Nanowires

The light absorption in single coaxial NWs of c-Si cores and a-Si shells can be well described within the framework of the Lorenz-Mie light scattering theory [43]. The term 'single' will be omitted hereafter if there is no confusion in this section. Such a hybrid system, which is a case of Fig. 3.1b, is simply characterized by the core radius r of c-Si, the shell thickness t of a-Si, and the total radius $R = r + t$. The cross section of the coaxial NWs is illustrated in Fig. 3.3a, together with the incident light perpendicular to the NW axis (thick arrows). The light absorption efficiency Q_{abs}, which is a measure of the capability to absorb light, can be obtained from equation 3.6
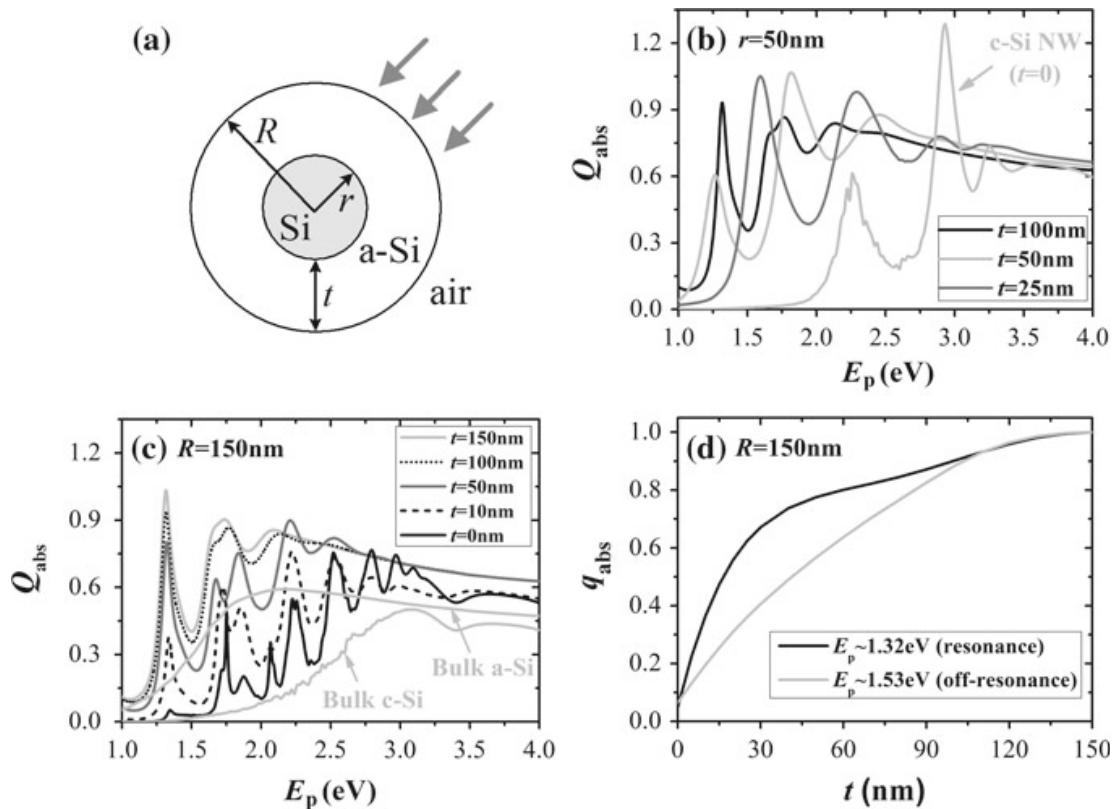
Fig. 3.3 a A schematic diagram of the cross section of coaxial NWs. *Thick arrows* indicate the incident light. **b** Q_{abs} versus E_p for various t at $r = 50$ nm. **c** Q_{abs} versus E_p for various t at $R = 150$ nm. Q_{abs} for bulk Si and bulk a-Si is shown for comparison. **d** Q_{abs} versus t at $E_p \sim 1.32$ and 1.53 eV. (Reproduced with permission from Liu et al. [53]. © 2011 IOP Publishing Ltd.)

for the coaxial NWs. For Q_{ab} calculations, the complex refractive indices of c-Si (m_2) and a-Si (m_1) were taken from [39].

The absorption efficiency Q_{abs} is presented versus photon energy E_p in Fig. 3.3b, in coaxial NWs of a fixed core radius ($r = 50$ nm) for various shell thicknesses ($t = 0$, 25, 50, and 100 nm) in air ($m_0 = 1$). Regardless of the shell thicknesses, there occur distinct absorption resonances even for c-Si NWs ($t = 0$), indicating that they do not simply come from the hybrid nature of coaxial NWs. These absorption resonances are in fact an interesting property of NWs, so-called leaky-mode resonances (LMRs) that can arise when light is incident onto subwavelength structures of high refractive indices, as will be discussed in detail later. In the figure, it has to be emphasized that the coaxial NWs ($t \neq 0$) have significantly enhanced light absorption for the weak absorption region ($E_p < 3.0$ eV) of the c-Si NWs ($t = 0$), likely due to the a-Si shells.

The absorption efficiency Q_{abs} is also presented versus photon energy E_p in Fig. 3.3c, in coaxial NWs of a fixed total radius ($R = 150$ nm) for various shell thicknesses ($t = 0$, 10, 50, 100, and 150 nm) in air, together with those in bulk c-Si and a-Si of 300 nm ($=2R$) thickness for comparison. Note that $t = 0$ and 150 nm represent c-Si and a-Si NWs of the radius 150 nm, respectively. The light absorption in the c-Si and a-Si NWs, as compared to in their bulk counterparts, is significantly enhanced for the entire solar band investigated ($E_p = 1.0 - 4.0$ eV) and, more importantly, this absorption enhancement is more significant for the weak absorption solar bands of the bulk materials ($E_p < 3.0$ eV for c-Si and < 1.8 eV for a-Si) mainly owing to the occurrence of absorption resonances in these NWs. As the a-Si shell thickness increases, on the other hand, the overall light absorption in the coaxial NWs is quickly enhanced and becomes rather saturated for $t > 100$ nm. Such saturating behavior can be clearly seen from Fig. 3.3d, which displays a scaled absorption efficiency $Q_{abs} = Q_{abs}(t)/Q_{abs}(t = 150 \text{ nm})$ at two representative photon energies, i.e., at $E_p \sim 1.53$ eV (off-resonance) and ~ 1.32 eV (resonance). Note that $Q_{abs}(t = 150 \text{ nm})$ is the absorption efficiency of the a-Si NWs of the radius 150 nm. The absorption efficiency of the coaxial NWs reaches $\sim 90\%$ of that of the a-Si NWs (90.1 % at $E_p \sim 1.32$ eV and 88.3 % at ~ 1.53 eV) at $t = 100$ nm ($=2r$). It is important to address that the light absorption of coaxial NWs can further increase up to additional $\sim 10\%$ for $t > 100$ nm, however, the performance of PV cells made of such coaxial NWs may be degraded due to the poor charge collection of thick a-Si shells: charge carrier diffusion lengths of a-Si ~ 100 nm. Thus, the saturating behavior of the absorption efficiency may help in designing coaxial NWs-based PV cells of enhanced light absorption (owing to the a-Si shells) with still high charge collection (owing to the c-Si cores).

The absorption resonance behavior of coaxial NWs presented above can be understood in terms of LMRs that may occur in subwavelength structures of high refractive indices such as semiconductor NWs [13, 32] and nanospheres [51]. For high-refractive index NWs, the incident light can be trapped in the NWs by multiple internal reflections, between which constructive interference arises and leads to LMRs when the wavelength λ of the incident light matches up with one of LMRs supported by the NWs. LMRs can be expressed as TM$_{ml}$ or TE$_{ml}$, where m and l are the azimuthal mode number and the radial order of LMRs, respectively. As in
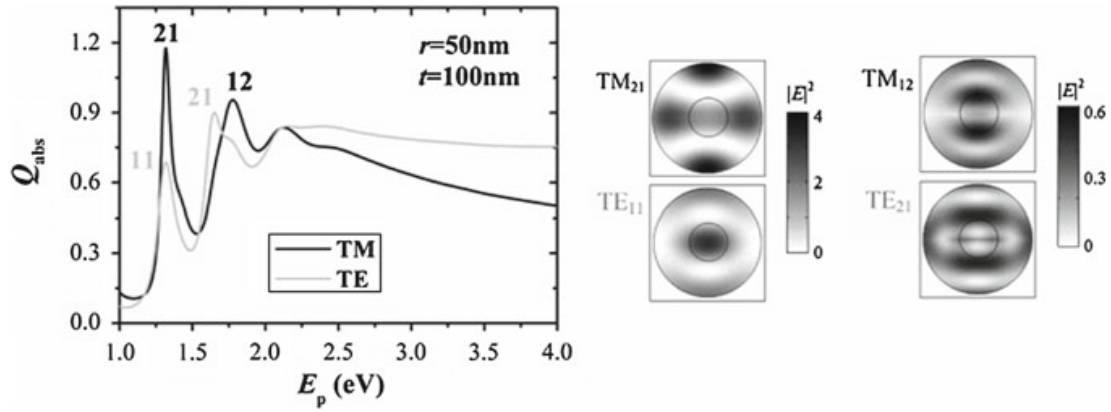
Fig. 3.4 (*Left*) Q_{abs} versus E_p at $r = 50\,\text{nm}$ and $t = 100\,\text{nm}$ for TM- and TE-polarized illuminations. (*Right*) Distributions of the electric field intensity $|E|^2$ (normalized to the incident light) inside the coaxial NWs are shown for the LMR peaks indicated. (Reproduced with permission from Liu et al. [53]. © 2011 IOP Publishing Ltd.)

Fig. 3.4, showing the absorption efficiency Q_{abs} for coaxial NWs of $r = 50\,\text{nm}$ and $t = 100\,\text{nm}$ under TM-/TE-polarized illumination, each absorption resonance corresponds to such a specific LMR as TM_{12}/TE_{21} (nondegenerate) near $E_p \sim 1.70\,\text{eV}$ ($\lambda \sim 730\,\text{nm}$) and TM_{21}/TE_{11} (exact degenerate) at $E_p \sim 1.32\,\text{eV}$ ($\lambda \sim 940\,\text{nm}$). Fig. 3.4 also shows the cross-sectional distributions of the electric field intensity $|E|^2$ inside the coaxial NWs at the resonance peaks. The amplitudes of $|E|^2$ are clearly stronger in the a-Si shells than in the c-Si cores. Thus, Fig. 3.4 provides compelling evidence that the incident light can be effectively trapped in the coaxial NWs through LMRs and also that the light absorption enhancement in the coaxial NWs arises owing to the a-Si shells.

The light absorption in coaxial NWs can be better seen from two-dimensional (2D) Q_{abs} maps, as plotted in Fig. 3.5, versus R and E_p at a fixed $g = 2$ for TM-/TE-polarized illumination, where g is defined as the ratio of the a-Si shell thickness to the c-Si core radius, i.e., $g = t/r$. Each absorption resonance corresponds to a LMR, as labeled in the figure. These 2D Q_{abs} maps provide extensive tunability of the light absorption in coaxial NWs. As the total radius R increases, there occur more LMRs and the position of each mode is shift to lower energy, indicating a redshift. At a given R, the coaxial NWs show relatively high absorption at a high photon energy region ($E_p > E_C$), e.g., $E_C \sim 1.32\,\text{eV}$ at $R = 150\,\text{nm}$, as indicated with an arrow in Fig. 3.5a. Such high absorption has also been reported in similar yet arrayed coaxial NWs [29]. Importantly, it is evident from the figure that the light absorption can be particularly high if the total radius R is tuned such that the light absorption spectrum contains TM_{01} (the strongest LMR) or TM_{11} (the second strongest LMR) mode, respectively.

The tunability of the light absorption gives a useful hint to design high-performance PV cells based on coaxial NWs. In order to investigate a potential benefit of such PV cells, one can calculate the photocurrent density or short-circuit current density J_{SC} in coaxial NWs as
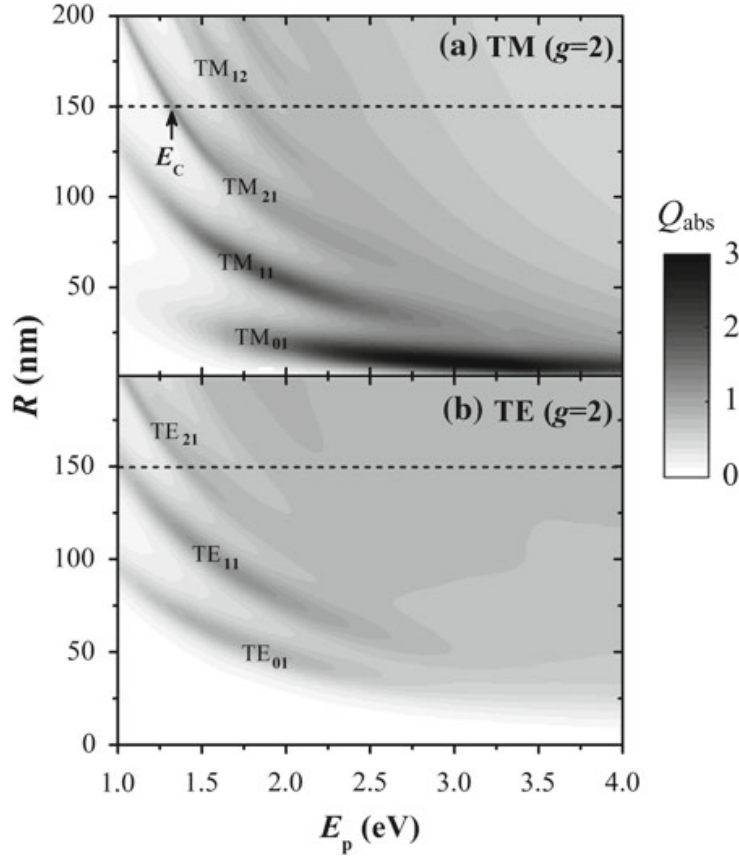
Fig. 3.5 Q_{abs} versus R and E_p at $g = 2$ for **a** TM- and **b** TE-polarized illuminations. The *dashed lines* represent the results shown in Fig. 3.4. LMRs are indicated. See text for E_c. (Reproduced with permission from Liu et al. [53]. © 2011 IOP Publishing Ltd.)

$$J_{SC}(R, g) = q \int Q_{abs}(E_P, R, g) F(E_P) dE_P, \tag{3.15}$$

where q is the elementary charge, $F(E_p)$ is the reference AM 1.5G spectra [52], and 100% charge collection efficiency is considered to obtain the ultimate photocurrent density. A 2D J_{SC} versus R and g is presented in Fig. 3.6a. At a given R, J_{SC} is fast enhanced with g increased and its enhancement then becomes slow for $g > 2$ (i.e., $t > 2r$), e.g., $J_{SC}(g = 2)$ reaches 93.6% of $J_{SC}(g \to \infty)$ at $R = 150$ nm, where $J_{SC}(g \to \infty)$ implies J_{SC} of a-Si NWs. In Fig. 3.6b, the R-dependent J_{SC} in the coaxial NWs is presented at a fixed $g = 2$, together with those in Si NWs, bulk Si, and bulk a-Si, having the same volume of materials, for comparison. The coaxial NWs can clearly produce much larger photocurrent than their counterparts. For example, the coaxial NWs yield $J_{SC} = 28.2$ mA/cm^2 at $R = 150$ nm (or $r = 50$ nm and $t = 100$ nm), which appears significant as compared to 8.5 mA/cm^2 in the Si NWs. Such photocurrent enhancement of the coaxial NWs with respect to the counterparts can be readily seen from Fig. 3.6c, where the photocurrent enhancement factor (PEF) is plotted versus R. The PEF is defined as $(I_{SC,cNW}/V_{cNW} - I_{SC,CP}/V_{CP})/(I_{SC,CP}/V_{CP})$, where $I_{SC,cNW}(V_{cNW})$ and
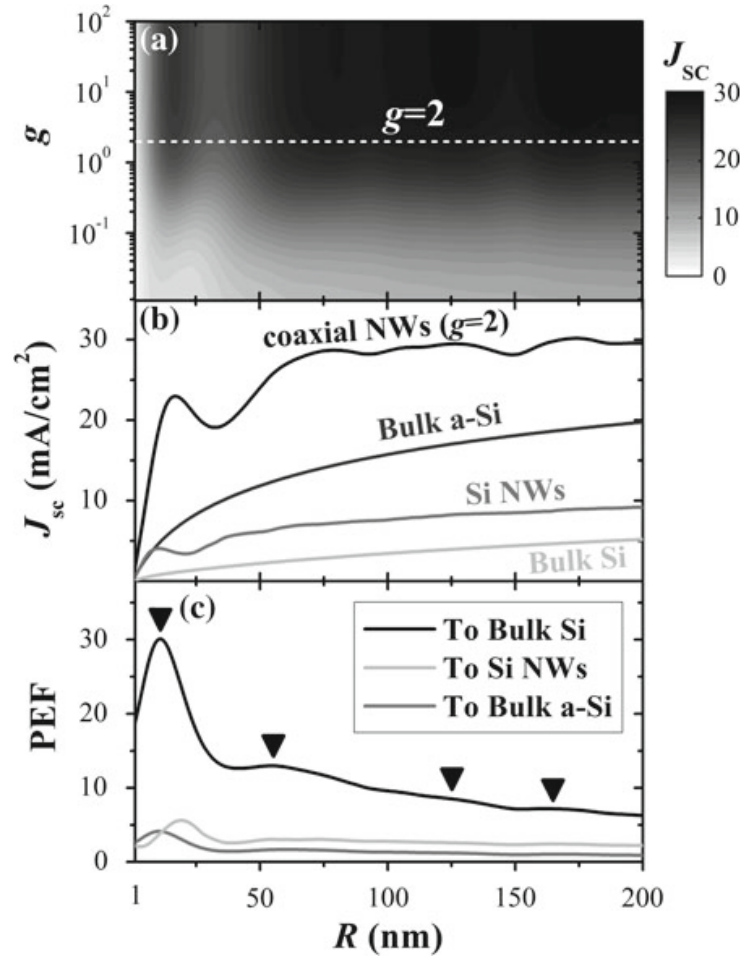
Fig. 3.6 **a** J_{sc} versus g and R. The *dashed line* indicates the case of $g = 2$. **b** J_{sc} versus R for coaxial NWs ($g = 2$), together with for Si NWs, bulk Si, and bulk a-Si for comparison. **c** PEF versus R with respect to Si NWs, bulk Si, and bulk a-Si. See text for *triangles*. (Reproduced with permission from Liu et al. [53]. © 2011 IOP Publishing Ltd.)

$I_{SC,CP}(V_{CP})$ are photocurrents (volumes) for the coaxial NWs ($g = 2$) and the counterparts (Si NWs, bulk Si, and bulk a-Si), respectively. The PEF curves with respect to the bulk counterparts exhibit a series of local maxima at certain R's as indicated with the triangles in Fig. 3.6c. These local maxima result primarily from the occurrence of such LMRs as TM_{01}, TM_{11}/TE_{01}, TM_{21}/TE_{11}, and TM_{12}/TE_{21} from the left to the right. At these R's (11, 55, 125, and 165 nm), the PEF against the bulk Si (bulk a-Si) are 30.1 (4.1), 13.0 (1.7), 8.5 (1.2), and 7.2 (1.0), respectively. Also, it ranges between 2.1 and 5.6 with respect to the Si NWs for the entire R investigated.

A practical use of coaxial NW PV cells may be limited since the electrical power generated is extremely low due to their nanoscale dimensions. They may be however still useful to power nanoelectronic devices that may require ultralow power. There has been a pioneer work recently, demonstrating that coaxial NW PV cells can serve as power sources to drive functional nanoelectronic sensors and logic gates [15]. The coaxial NW PV cells were made of *p*-type c-Si cores, intrinsic nanocrystalline Si
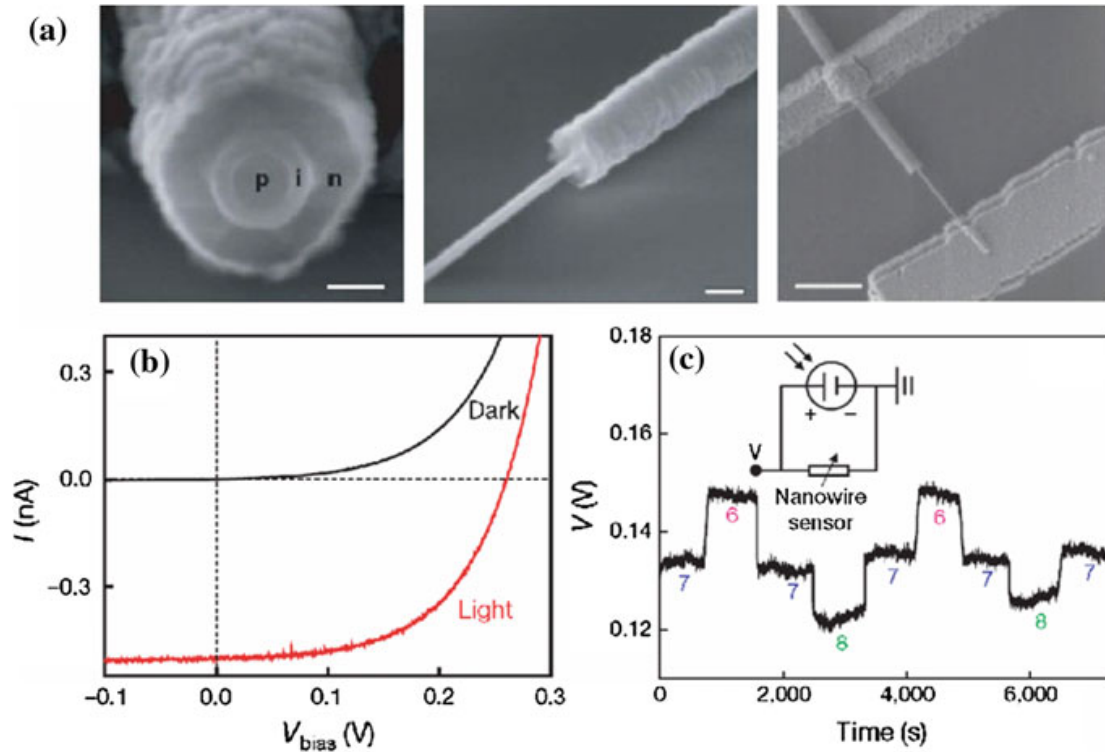
Fig. 3.7 **a** SEM images of a coaxial NW PV cell: (*left*) *p*-type c-Si core, intrinsic nc-Si shell, and *n*-type nc-Si shell. (middle) selective etching to expose the *p*-core. (*right*) metal contacts deposited on the *p*-core and *n*-shell. *Scale bars* are 100 nm (*left*), 200 nm (*middle*), and 1.5 μm (*right*). **b** Dark and light I–V curves. **c** Real-time detection of the voltage drop across an aminopropyltriethoxysilane-modified silicon nanowire at different pH values. The silicon nanowire pH sensor is powered by a coaxial NW PV cell operating under 8-sun illumination ($V_{oc} = 50.34$ V, $I_{sc} = 58.75$ nA). *Inset* shows circuit schematics. (Reprinted with permission from Tian et al. [15]. © 2007 Nature Publishing Group.)

(nc-Si) shells, and n-type nc-Si shells, as shown in Fig. 3.7a. *I-V* curves are also shown in Fig. 3.7b, providing that an open-circuit voltage V_{OC} of 0.260 V, a short-circuit current I_{SC} of 0.503 nA, a fill factor of 55.0 %, and the maximum power output of 72 pW at 1-sun. The upper bound of a short-circuit current density estimated was about 23.9 mA/cm^2, similar to our calculated result (28.2 mA/cm^2 at $R = 150$ nm) presented above. Importantly, the functionality of the coaxial NW PV cells has been demonstrated to power a nanoelectronic sensor, as can be seen from Fig. 3.7c.

Although the coaxial NW PV cells may not be used for large-scale power generation, the light trapping mechanism in coaxial NWs may help in designing large-scale PV cells. A feasible way is to make use of planar semi-coaxial NW arrays, as illustrated in Fig. 3.8. Such planar NW arrays can be fabricated on c-Si wafers by means of current lithography technique (for c-Si cores) combined with chemical vapor deposition (for a-Si shells). The underlying mechanism of light absorption in planar NW arrays may not be expected to be much different from that in the single coaxial NWs (i.e., LMRs) discussed above, except that coupled LMRs might be considered if neighboring NWs are too close [33]. The optimal dimensions of the planar NW
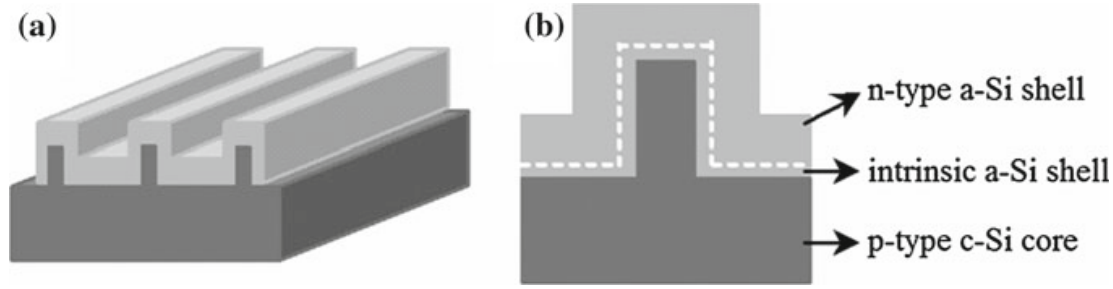
Fig. 3.8 Schematic illustrations of wafer-scale PV cells made of planar semi-coaxial NW arrays. **a** Overall look. **b** *Side view*, showing *p*-type c-Si core, intrinsic a-Si shell, and *n*-type a-Si shell

arrays for PV applications, however, need to be further investigated, which is beyond the scope of this chapter.

3.4 Light Trapping in Coaxial Nanowire Arrays

The light absorption in coaxial NW arrays of c-Si cores and a-Si:H shells can be numerically calculated by the RCWA method [44–46]. Here, vertically aligned square arrays in air are considered, which are a case of the 2D grating depicted in Fig. 3.2, so that the regions I and II can be treated as air, the pitch $p = p_x = p_y$, and the length of the NWs $L = d$. Such coaxial NW arrays are simply characterized by the pitch p, the length L, the core radius r of c-Si, the total radius R (or the a-Si:H shell thickness $t = R - r$), and the filling ratio $f = \pi R^2/p^2$. For RCWA simulations, TE- and TM-polarized lights were considered to be incident at an angle of θ in the $x - z$ plane ($\phi = 0$ in Fig. 3.2a) and the complex refractive indices of c-Si ($m_2 = \varepsilon_2^{1/2}$ in Fig. 3.2c) and a-Si:H ($m_3 = \varepsilon_3^{1/2}$ in Fig. 3.2c) were taken from [39].

Absorptance and reflectance are presented versus photon energy E_p in Fig. 3.9, in coaxial NW arrays of $p = 200$ nm, $r = 50$ nm, and $L = 1.0\,\mu$m for various shell thicknesses ($t = 0 - 50$ nm, corresponding to the filling ratio $f = 0.196 - 0.785$) at $\theta = 0°$ (i.e., parallel to the z axis or the NW axis). As shown in the top panel of Fig. 3.9a, the light absorption in c-Si NW arrays ($t = 0$) is clearly enhanced for high photon energy ($E_p > 2.5$ eV) compared to in c-Si thin films, likely resulting from lower reflection in the former than in the latter (see the top panel of Fig. 3.9b). This absorption enhancement may be associated with intrinsically lower reflection in c-Si NW arrays due to their open structure. The NW array structure has a large open area, naturally leading to low reflection that perhaps results in high absorption. This absorption enhancement may also be associated with interwire light scattering [10, 27], which occurs when dimensions of NW arrays (diameter and pitch) are comparable to the wavelength of incident light, elongating the optical path length. Although it is enhanced for the high photon energy, the light absorption in c-SiNW arrays remarkably drops for the photon energy range of 1.5–2.5 eV that is the most important solar band for PV applications. This absorption drop has been known to
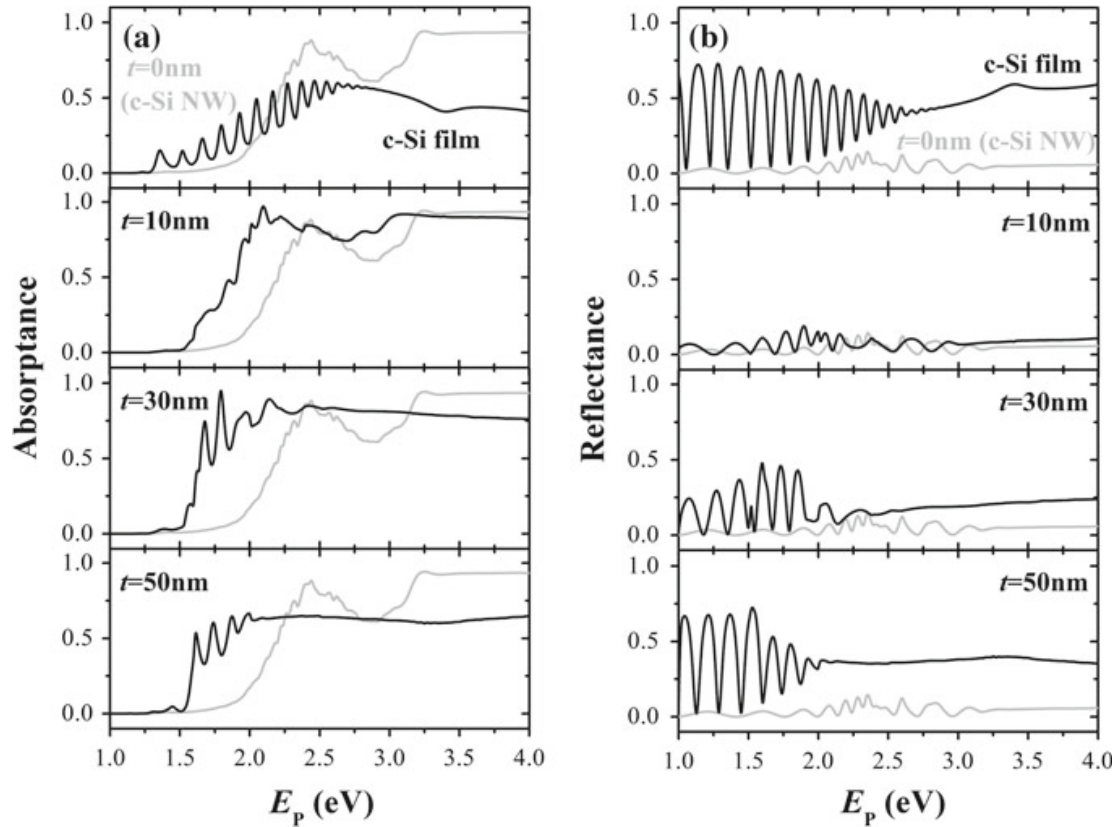
Fig. 3.9 **a** Absorptance and **b** reflectance versus E_p for various t at $p = 200$ nm, $r = 50$ nm, $L = 1.0\,\mu$m, and $\theta = 0°$. (Reproduced with permission from Xie et al. [54]. © 2011 American Institute of Physics.)

come from the indirect bandgap nature of c-Si that leads to a poor capability to absorb low energy photons ($E_p < 2.5$ eV) [19]. Although this low energy absorption suppression has been known to be improved to some extent by tuning the geometry of NW arrays (length, diameter, or/and pitch), its improvement is rather limited [19–21].

It is evident in Fig. 3.9a that the light absorption in c-SiNW arrays for the low energy (1.5–2.5 eV) is significantly reinforced by coating a small amount of a-Si:H ($t = 10$ nm). Such absorption reinforcement in coaxial NW arrays may be expected from the fact that the imaginary part of complex refractive index, which is proportional to the absorption coefficient, is ~10 times bigger in a-Si:H than in c-Si for the low energy: e.g., it is 0.217 (0.022) for a-Si:H (c-Si) at $E_p = 2.0$ eV [39]. As the shell thickness increases to 30 nm, the light absorption is further enhanced mainly owing to distinct absorption resonances. For a further increase of the shell thickness to 50 nm, however, the overall absorption becomes smaller than that for $t = 30$ nm, since a larger material filling ratio for $t = 50$ nm leads to a smaller open area which then results in larger reflection as can be seen in Fig. 3.9b. It has to be emphasized here that the distinct absorption resonances, which are in fact LMRs discussed below, are clearly a major source of the absorption enhancement in coaxial NW arrays for the low photon energy. In Fig. 3.10a, the E_p-dependent absorptance is presented for coaxial NW arrays ($R = 80$ nm, $r = 50$ nm, and $L = 1.0\,\mu$m), c-Si NW arrays
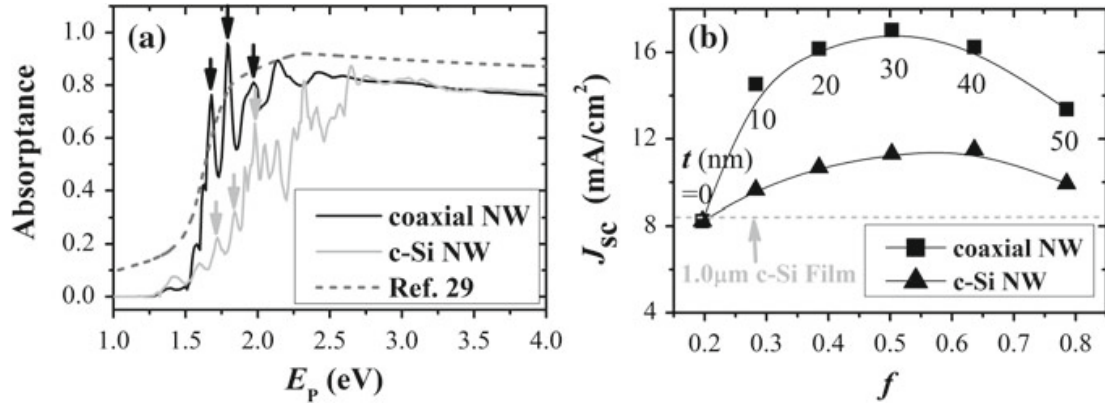
Fig. 3.10 **a** Absorptance versus E_p for coaxial NW arrays ($R = 80$ nm, $t = 30$ nm) and c-Si NW arrays ($r = 80$ nm) at $p = 200$ nm, $L = 1.0$ μm, and $\theta = 0°$, together with for disordered coaxial NW arrays ($R = 74$–90 nm, $r = 15$–30 nm, $L = 1.282$ μm from [29]). **b** J_{SC} versus f for coaxial NW arrays ($r = 50$ nm) and c-Si NW arrays at $p = 200$ nm, $L = 1.0$ μm, and $\theta = 0°$, together with for c-Si thin film of 1.0 μm thick. (Reproduced with permission from Xie et al. [54]. © 2011 American Institute of Physics.)

($r = 80$ nm and $L = 1.0$ μm), and disordered coaxial NW arrays ($R = 74$–90 nm, $r = 15$–30 nm, and $L = 1.282$ μm from [29]). The amplitudes of resonances indicted with arrows are evidently bigger in the coaxial NW arrays than the c-Si NW arrays, similar to a behavior of LMRs occurring in the single coaxial NW system discussed in the previous section. The number of resonance peaks is less in the coaxial NW arrays than in the c-Si NW arrays, also similar to another behavior of LMRs occurring in the single coaxial NW system. Interestingly, absorption resonances won't occur in the disordered coaxial NW arrays [29], implying that absorption resonances appear to be a signature of ordered NW arrays.

In addition to a large open area and the interwire light scattering as mentioned above, absorption resonances evidently play an important role in the absorption enhancement in coaxial NW arrays. As discussed in the previous section, LMRs occur and serve as a primary source to trap light in the single NW system. Furthermore, LMRs have recently been shown to be a major source of absorption enhancement in the NW array system [34]. Note that, in this chapter, the incident light is considered to be perpendicular to the NW axis in the case of the single coaxial NW system, whereas it is parallel to the NW axis in the case of the coaxial NW array system. Although the configuration of incident light versus the NW axis results in different kinds of excitation of LMRs, i.e., TM and TE modes (perpendicular) and hybrid TM-dominant HE modes (parallel) [34], a primary role of LMRs in the light absorption is essentially same for both cases. Note also that LMRs, which result from the interaction between light and subwavelength matters, are physically different from Fabry-Pérot resonances, which come from interference between multiple reflections of light from two reflecting surfaces. The latter is typically observed in c-Si thin films (see regular interference patterns in the top panels of Fig. 3.9).

As in single coaxial NWs, one can calculate the ultimate photocurrent density or short-circuit current density J_{SC} to evaluate the absorption enhancement in coaxial NW arrays for photovoltaic applications as

$$J_{SC}(f, p) = q \int A(E_P, f, p) F(E_P) dE_P, \qquad (3.16)$$

which is the same equation as equation 3.15, expressed with absorptance A instead of absorption efficiency Q_{abs}. The f-dependent (or t-dependent) J_{SC} is presented in Fig. 3.10b, in coaxial NW arrays of $r = 50$ nm, $p = 200$ nm, and $L = 1.0 \mu m$. J_{SC} in the coaxial NW arrays has the maximum of 17.0 mA/cm^2 at $f = 0.5$ (or $t = 30$ nm), at which J_{SC} is 11.3 mA/cm^2 (8.5 mA/cm^2) in c-SiNW arrays of the same dimensions (c-Si thin film of 1.0 μm thick). At this optimal filling ratio $f = 0.5$, the light absorption in the coaxial NW arrays is highest as can be seen in Fig. 3.9a. As a result, the PEF of the coaxial NW arrays is about 0.5 (3.0) with respect to the c-SiNW arrays (c-Si thin film).

To further investigate the optimal geometry of coaxial NW arrays for PV applications, absorptance and reflectance are shown versus E_p in Fig. 3.11, in coaxial NW arrays of $f = 0.5$, $r/p = 1/4$, and $L = 1.0 \mu m$ for various pitches ($p = 100$–900 nm, corresponding to $t = 14.9$–134.1 nm) at $\theta = 0°$. The top views of coaxial NW arrays with different pitches are schematically shown in Fig. 3.12a. For the smallest pitch ($p = 100$ nm), the absorption spectrum exhibits a clifflike behavior: a plateau of high absorption ($A = 80 \sim 87\%$), a cliff edge ($E_{CE} \sim 2.0$ eV), and a sharp cliff hill.
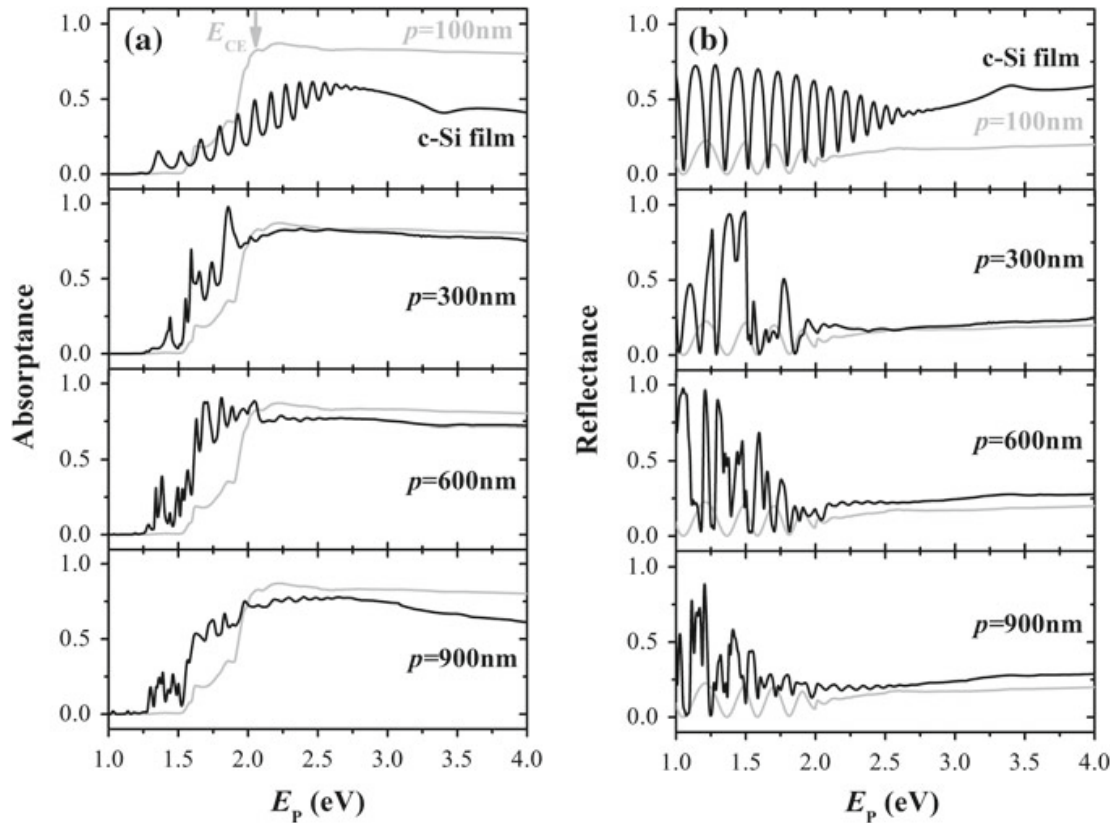
**Fig. 3.11 a** Absorptance and **b** reflectance versus E_p for various p at $f = 1/2$, $r/p = 1/4$, $L = 1.0 \mu m$, and $\theta = 0°$. See texts for E_{CE}. (Reproduced with permission from Xie et al. [54]. © 2011 American Institute of Physics.)
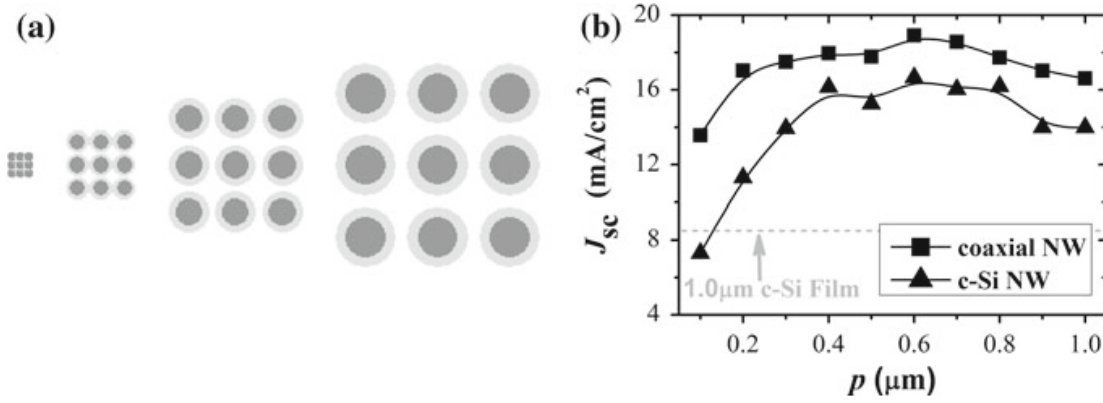
Fig. 3.12 **a** Schematic top views of coaxial NW arrays with $p = 100, 300, 600, 900\,\mathrm{nm}$ from *left* to *right* at $f = 1/2$ and $r/p = 1/4$. **b** J_{SC} versus p for coaxial NW arrays ($r/p = 1/4$) and c-Si NW arrays [$r/p = (1/2\pi)^{1/2}$] at $f = 1/2$, $L = 1.0\,\mu\mathrm{m}$, and $\theta = 0°$, together with for c-Si thin film of $1.0\,\mu\mathrm{m}$ thick. (Fig. 3.12b is reproduced with permission from Xie et al. [54]. © 2011 American Institute of Physics.)

For $p = 300$ and $600\,\mathrm{nm}$, the absorption resonances strongly occur along the cliff hill and the cliff edge clearly becomes shifted to the low energy (e.g., $E_{CE} \sim 1.5\,\mathrm{eV}$ for $p = 600\,\mathrm{nm}$), leading to absorption enhancement. For $p = 900\,\mathrm{nm}$, however, the overall absorption is evidently smaller than that for $p = 600\,\mathrm{nm}$. Very interestingly, the p-dependent reflectance behaves just like the absorptance, i.e., it increases as $p = 100 \rightarrow 600\,\mathrm{nm}$ and decreases as $p = 600 \rightarrow 900\,\mathrm{nm}$. This implies that the incident light becomes more effectively trapped into coaxial NW arrays through LMRs as $p = 100 \rightarrow 600\,\mathrm{nm}$ so that it is less transmitted. Also, the absorption drop for $p = 600 \rightarrow 900\,\mathrm{nm}$ has to result from transmission increase, since the overall reflection for $p = 900\,\mathrm{nm}$ is slightly smaller than that for $p = 600\,\mathrm{nm}$. This implies that such subwavelength light-trapping effect diminishes as the pitch becomes larger ($p = 600 \rightarrow 900\,\mathrm{nm}$), in good agreement with [38]. The optimal pitch of coaxial NW arrays for photovoltaic applications is clearly seen to be $\sim 600\,\mathrm{nm}$ from Fig. 3.12b, which shows the p-dependent J_{SC} in coaxial NW arrays. At this optimal pitch $p = 600\,\mathrm{nm}$, J_{SC} in coaxial NW arrays reaches the maximum of $18.9\,\mathrm{mA/cm^2}$, whereas J_{SC} is $16.6\,\mathrm{mA/cm^2}$ ($8.5\,\mathrm{mA/cm^2}$) in c-SiNW arrays (c-Si thin film of $1.0\,\mu\mathrm{m}$ thick). Thus, the PEF of the coaxial NW arrays is about 0.14 (3.45) with respect to the c-SiNW arrays (c-Si thin film).

To examine the effect of the NW length L of coaxial NW arrays on the light absorption or the photocurrent density, J_{SC} is plotted versus L in Fig. 3.13a at the optimal filling ratio ($f = 0.5$) and pitch ($p = 600\,\mathrm{nm}$). The L-dependent J_{SC} in coaxial NW arrays sharply increases as L varies from 0.1 to $5.0\,\mu\mathrm{m}$ and shows a gradually growing behavior for a further increase of L. To also examine the effect of the incident angle θ of light on the light absorption, J_{SC} in the $1.0\,\mu\mathrm{m}$-length coaxial NW arrays is plotted versus θ at the optimal configuration ($f = 0.5$ and $p = 600\,\mathrm{nm}$) for the TE and TM polarizations in Fig. 3.13b, together with for the unpolarized light that is simply an average value of those for TE and TM. It is evident from the figure that the photocurrent density is maintained at a high constant ($\sim 20\,\mathrm{mA/cm^2}$) over a
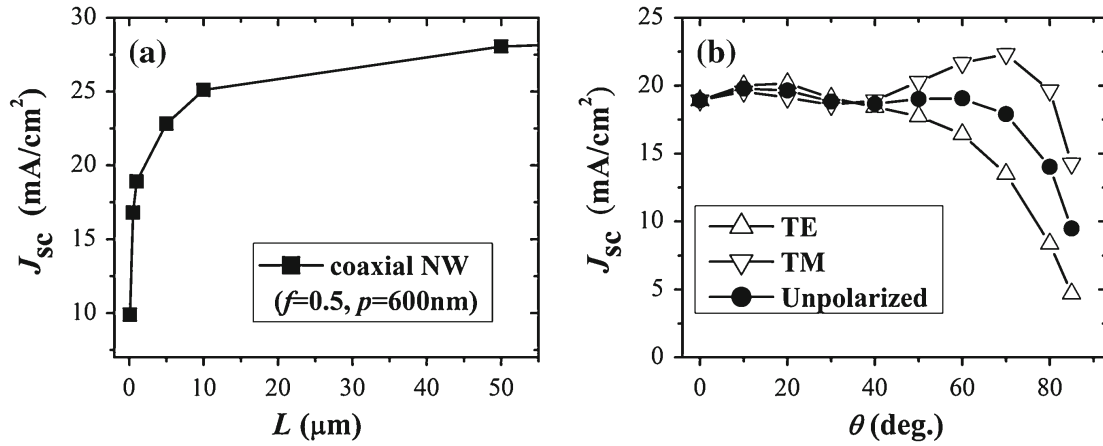
Fig. 3.13 **a** J_{SC} versus L at $f = 0.5$, $p = 600\,\text{nm}$, and at $\theta = 0°$. **b** J_{SC} versus θ for TE-, TM-, and unpolarized-illuminations at $f = 0.5$, $p = 600\,\text{nm}$, and $L = 1.0\,\mu\text{m}$. (Reproduced with permission from Xie et al. [54]. © 2011 American Institute of Physics.)
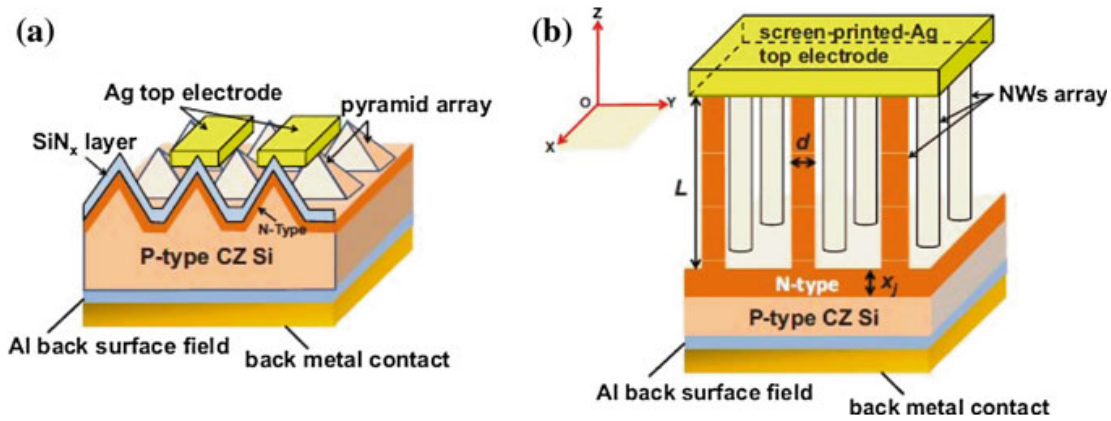
Fig. 3.14 The three-dimensional schematic view of (**a**) the conventional pyramid-array-textured c-Si solar cells and (**b**) the Si NW-array-textured solar cells, in which L represents the length of the NWs, d is the diameter of the single NW, and X_j is the junction depth of the p-n junction after phosphorus diffusion. (Reprinted with permission from Chen et al. [30]. © 2010 American Institute of Physics.)

large range of the incident angle of light ($\theta = 0-70°$), indicating an omnidirectional light absorption in coaxial NW arrays. Note that the absorption difference between the cases of the incident light in and out-of the x-z plane is known to be negligible [19].

Coaxial NW arrays may be practically used as a light absorbing layer in wafer-scale PV cells. There has been a recent work, fabricating c-Si NW-textured PV cells [30]. There, c-Si NW arrays replaced conventional pyramid-textured layers, as shown in Fig. 3.14. Such NW-array-textured wafer-scale ($125 \times 125\,\text{mm}^2$) PV cells (Fig. 3.14b) had a 16.5 % power conversion efficiency, which was 35.4 % enhancement as compared to the pyramid-textured control PV cells (Fig. 3.14a). That enhancement turned out to come from significant absorption enhancement of c-Si NW arrays. Nonetheless, more efforts need to be made to develop high-performance

PV cells based on NW arrays. The light absorption properties of coaxial NW arrays discussed in this section could help in designing high-performance NW-based PV cells.

3.5 Summary and Conclusions

The light-trapping scheme has been investigated in coaxial NWs of c-Si cores and a-Si shells for both cases of single coaxial NWs and coaxial NW arrays. Based on numerical calculations, it has been shown that the incident light can be effectively trapped in the coaxial NWs through the excitation of LMRs as in other NWs and the a-Si shells play a primary role in enhancing the light absorption in the coaxial NWs as compared to in the c-Si NWs of same geometric dimensions. It has been further shown that the light absorption in the coaxial NWs can be optimized by tuning the dimensions of the coaxial NWs. For the single coaxial NWs, the light absorption is optimized when the thickness of the a-Si shell is about as twice as the radius of the Si core, at which the ultimate photocurrent can be enhanced up to 560 % in comparison with that in the single c-Si NWs. As for the coaxial NW arrays, on the other hand, the optimal absorption occurs when the coaxial NWs are about half-filled and the pitch is about 600 nm, at which it can be increased up to 14 % with the 1 μm long NWs considered, as compared to that in the c-Si NW arrays. The effective light-trapping scheme in the coaxial NWs together with the absorption optimization results can provide opportunities for designing not only functional power sources of nanoelectronic devices but also next generation PV cells.

References

1. Nelson, J.: The Physics of Solar Cells. Imperial College Press, London (2003)
2. Dale, B., Rudenberg, H.G.: High efficiency silicon solar cells. In: Proceedings of the 14th Annual Power Sources Conference, p 22 (1960)
3. Pillai, S., Catchpole, K.R., Trupke, T., Green, M.A.: Surface plasmon enhanced silicon solar cells. J. Appl. Phys. **101**, 093105 (2007)
4. Beck, F.J., Polman, A., Catchpole, K.R.: Tunable light trapping for solar cells using localized surface plasmons. J. Appl. Phys. **105**, 114310 (2009)
5. Ferry, V.E., Verschuuren, M.A., Li, H.B.B.T., Schropp, R.E.I., Atwater, H.A., Polman, A.: Improved red-response in thin film a-Si:H solar cells with soft-imprinted plasmonic back reflectors. Appl. Phys. Lett. **95**, 183503 (2009)
6. Atwater, H.A., Polman, A.: Plasmonics for improved photovoltaic devices. Nat. Mater. **9**, 205–213 (2010)

7. Ferry, V.E., Verschuuren, M.A., Li, H.B.B.T., Verhagen, E., Walters, R.J., Schropp, R.E.I., Atwater, H.A., Polman, A.: Light trapping in ultrathin plasmonic solar cells. Opt. Express **18**, A237–A245 (2010)
8. Chen, X., Jia, B.H., Saha, J.K., Cai, B.Y., Stokes, N., Qiao, Q., Wang, Y.Q., Shi, Z.R., Gu, M.: Broadband enhancement in thin-film amorphous silicon solar cells enabled by nucleated silver nanoparticles. Nano Lett. **12**, 2187–2192 (2012)
9. Nunomura, S., Minowa, A., Sai, H., Kondo, M.: Mie scattering enhanced near-infrared light response of thin-film silicon solar cells. Appl. Phys. Lett. **97**, 063507 (2010)
10. Muskens, O.L., Rivas, J.G., Algra, R.E., Bakkers, E.P.A.M., Lagendijk, A.: Design of light scattering in nanowire materials for photovoltaic applications. Nano Lett. **8**, 2638–2642 (2008)
11. Cao, L.Y., White, J.S., Park, J.S., Schuller, J.A., Clemens, B.M., Brongersma, M.L.: Engineering light absorption in semiconductor nanowire devices. Nat. Mater. **8**, 643–647 (2009)
12. Pei, Z.W., Chang, S.T., Liu, C.W., Chen, Y.C.: Numerical simulation on the photovoltaic behavior of an amorphous-silicon nanowire-array solar cell. IEEE. Electron Device Lett. **30**, 1305–1307 (2009)
13. Liu, W.F., Oh, J.I., Shen, W.Z.: Light trapping in single coaxial nanowires for photovoltaic applications. IEEE. Electron Device Lett. **32**, 45–47 (2010)
14. Diedenhofen, S.L., Janssen, O.T.A., Grzela, G., Bakkers, E.P.A.M., Rivas, J.G.: Strong geometrical dependence of the absorption of light in arrays of semiconductor nanowires. ACS Nano. **5**, 2316–2323 (2011)
15. Tian, B.Z., Zheng, X.L., Kempa, T.J., Fang, Y., Yu, N.F., Yu, G.H., Huang, J.L., Lieber, C.M.: Coaxial silicon nanowires as solar cells and nanoelectronic power sources. Nature **449**, 885–890 (2007)
16. Kempa, T.J., Tian, B.Z., Kim, D.R., Hu, J.S., Zheng, X.L., Lieber, C.M.: Single and tandem axial p-i-n nanowire photovoltaic devices. Nano Lett. **8**, 3456–3460 (2008)
17. Tian, B.Z., Kempa, T.J., Lieber, C.M.: Single nanowire photovoltaics. Chem. Soc. Rev. **38**, 16–24 (2009)
18. Kim, S.K., Day, R.W., Cahoon, J.F., Kempa, T.J., Song, K.D., Park, H.G., Lieber, C.M.: Tuning light absorption in core/shell silicon nanowire photovoltaic devices through morphological design. Nano Lett. **12**, 4971–4976 (2012)
19. Hu, L., Chen, G.: Analysis of optical absorption in silicon nanowire arrays for photovoltaic applications. Nano Lett. **7**, 3249–3252 (2007)
20. Lin, C.X., Povinelli, M.L.: Optical absorption enhancement in silicon nanowire arrays with a large lattice constant for photovoltaic applications. Opt. Express **17**, 19371–19381 (2009)
21. Li, J.S., Yu, H.Y., Wong, S.M., Li, X.C., Zhang, G., Lo, P.G.Q., Kwong, D.L.: Design guidelines of periodic Si nanowire arrays for solar cell application. Appl. Phys. Lett. **95**, 243113 (2009)
22. Tsakalakos, L., Balch, J., Fronheiser, J., Korevaar, B.A., Sulima, O., Rand, J.: Silicon nanowire solar cells. Appl. Phys. Lett. **91**, 233117 (2007)
23. Stelzner, T., Pietsch, M., Andrä, G., Falk, F., Ose, E., Christiansen, S.: Silicon nanowire-based solar cells. Nanotechnology **19**, 295203 (2008)
24. Fang, H., Li, X.D., Song, S., Xu, Y., Zhu, J.: Fabrication of slantingly-aligned silicon nanowire arrays for solar cell applications. Nanotechnology **19**, 255703 (2008)
25. Garnett, E.C., Yang, P.D.: Silicon nanowire radial p-n junction solar cells. J. Am. Chem. Soc. **130**, 9224–9225 (2008)
26. Gunawan, O., Guha, S.: Characteristics of vapor-liquid-solid grown silicon nanowire solar cells. Sol. Energy Mater. Sol. Cells **93**, 1388–1393 (2009)
27. Bao, H., Ruan, X.L.: Optical absorption enhancement in disordered vertical silicon nanowire arrays for photovoltaic applications. Opt. Lett. **35**, 3378–3380 (2010)
28. Garnett, E., Yang, P.D.: Light trapping in silicon nanowiresolar cells. Nano Lett. **10**, 1082–1087 (2010)
29. Adachi, M.M., Anantram, M.P., Karim, K.S.: Optical properties of crystalline-amorphous core-shell silicon nanowires. Nano Lett. **10**, 4093–4098 (2010)
30. Chen, C., Jia, R., Yue, H.H., Li, H.F., Liu, X.Y., Wu, D.Q., Ding, W.C., Ye, T.C., Kasai, S., Tamotsu, H., Chu, J.H., Wang, S.L.: Silicon nanowire-array-textured solar cells for photovoltaic application. J. Appl. Phys. **108**, 094318 (2010)

31. Xie, W.Q., Oh, J.I., Shen, W.Z.: Realization of effective light trapping and omnidirectional antireflection in smooth surface silicon nanowirearrays. Nanotechnology **22**, 065704 (2011)
32. Cao, L.Y., Fan, P.Y., Vasudev, A.P., White, J.S., Yu, Z.F., Cai, W.S., Schuller, J.A., Fan, S.H., Brongersma, M.L.: Semiconductor nanowireoptical antenna solar absorbers. Nano Lett. **10**, 439–445 (2010)
33. Cao, L.Y., Fan, P.Y., Brongersma, M.L.: Optical coupling of deep-subwavelength semiconductor nanowires. Nano Lett. **11**, 1463–1468 (2011)
34. Wang, B., Leu, P.W.: Tunable and selective resonant absorption in vertical nanowires. Opt. Lett. **37**, 3756–3758 (2012)
35. Kelzenberg, M.D., Boettcher, S.W., Petykiewicz, J.A., Turner-Evans, D.B., Putnam, M.C., Warren, E.L., Spurgeon, J.M., Briggs, R.M., Lewis, N.S., Atwater, H.A.: Enhanced absorption and carrier collection in Si wire arrays for photovoltaic applications. Nat. Mater. **9**, 239–244 (2010)
36. Yablonovitch, E.: Statistical ray optics. J. Opt. Soc. Am. **72**, 899–907 (1982)
37. Tiedje, T., Yablonovitch, E., Cody, G.D., Brooks, B.G.: Limiting efficiency of silicon solar-cells. IEEE Trans. Electron Devices **31**, 711–716 (1984)
38. Kosten, E.D., Warren, E.L., Atwater, H.A.: Ray optical light trapping in silicon microwires: exceeding the 2 n^2 intensity limit. Opt. Express **19**, 3316–3331 (2011)
39. Palik, E.D.: Handbook of optical constants of solids. Academic Press, London (1985)
40. Shah, A.V., Schade, H., Vanecek, M., Meier, J., Vallat-Sauvain, E., Wyrsch, N., Kroll, U., Droz, C., Bailat, J.: Thin-film silicon solar cell technology. Prog. Photovolt. **12**, 113–142 (2004)
41. Dong, Y.J., Yu, G.H., McAlpine, M.C., Lu, W., Lieber, C.M.: Si/a-Si core/shell nanowires as nonvolatile crossbar switches. Nano Lett. **8**, 386–391 (2008)
42. Taguchi, M., Kawamoto, K., Tsuge, S., Baba, T., Sakata, H., Morizane, M., Uchihashi, K., Nakamura, N., Kiyama, S., Oota, O.: HIT^{TM} cells-high-efficiency crystalline Si cells with novel structure. Prog. Photovolt. **8**, 503–513 (2000)
43. Bohren, C.F., Huffman, D.R.: Absorption and scattering of light by small particles. Wiley, New York (1998)
44. Moharam, M.G., Gaylord, T.K.: Rigorous coupled-wave analysis of planar-grating diffraction. J. Opt. Soc. Am. **71**, 811–818 (1981)
45. Moharam, M.G., Grann, E.B., Pommet, D.A., Gaylord, T.K.: Formulation for stable and efficient implementation of the rigorous coupled-wave analysis of binary gratings. J. Opt. Soc. Am. A **12**, 1068–1076 (1995)
46. Moharam, M.G., Pommet, D.A., Grann, E.B., Gaylord, T.K.: Stable implementation of the rigorous coupled-wave analysis for surface-relief gratings: enhanced transmittance matrix approach. J. Opt. Soc. Am. A **12**, 1077–1086 (1995)
47. Brönstrup, G., Jahr, N., Leiterer, C., Csáki, A., Fritzsche, W., Christiansen, S.: Optical properties of individual silicon nanowires for photonic devices. ACS Nano **4**, 7113–7122 (2010)
48. Zhu, J., Yu, Z.F., Burkhard, G.F., Hsu, C.M., Connor, S.T., Xu, Y.Q., Wang, Q., McGehee, M., Fan, S.H., Cui, Y.: Optical absorption enhancement in amorphous silicon nanowire and nanocone arrays. Nano Lett. **9**, 279–282 (2009)
49. Lee, Y.J., Ruby, D.S., Peters, D.W., McKenzie, B.B., Hsu, J.W.P.: ZnO nanostructures as efficient antireflection layers in solar cells. Nano Lett. **8**, 1501–1505 (2008)
50. Chiu, C.H., Yu, P.C., Kuo, H.C., Chen, C.C., Lu, T.C., Wang, S.C., Hsu, S.H., Cheng, Y.J., Chang, Y.C.: Broadband and omnidirectional antireflection employing disordered GaN nanopillars. Opt. Express **16**, 8748–8754 (2008)
51. Khoury, C.G., Norton, S.J., Vo-Dinh, T.: Investigating the plasmonics of a dipole-excited silver nanoshell: Mie theory versus finite element method. Nanotechnology **21**, 315203 (2010)
52. Air Mass 1.5 Spectra. American society for testing and materials (http://rredc.nrel.gov/solar/spectra/am1.5/) (2012)
53. Liu, W.F., Oh, J.I., Shen, W.Z.: Light absorption mechanism in single c-Si (core)/a-Si (shell) coaxial nanowires. Nanotechnology **22**, 125705 (2011)
54. Xie, W.Q., Liu, W.F., Oh, J.I., Shen, W.Z.: Optical absorption in c-Si/a-Si:H core/shell nanowire arrays for photovoltaic applications. Appl. Phys. Lett. **99**, 033107 (2011)